Stratospheric Water Vapor from the Hunga Tonga–Hunga Ha'apai Volcanic Eruption Deduced from COSMIC-2 Radio Occultation

William J. Randel, Benjamin R. Johnston, John J. Braun, Sergey Sokolovskiy, Holger Vömel, Aurelien Podglajen, Bernard Legras

remote sensing

MDPI

Article

Stratospheric Water Vapor from the Hunga Tonga–Hunga Ha'apai Volcanic Eruption Deduced from COSMIC-2 Radio Occultation

William J. Randel [1,2,*], Benjamin R. Johnston [2], John J. Braun [2], Sergey Sokolovskiy [2], Holger Vömel [1], Aurelien Podglajen [3] and Bernard Legras [3]

[1] National Center for Atmospheric Research, Boulder, CO 80301, USA
[2] COSMIC Program Office, University Corporation for Atmospheric Research, Boulder, CO 80301, USA
[3] Laboratoire de Météorologie Dynamique (LMD-IPSL), UMR CNRS 8539, ENS-PSL, École Polytechnique, Sorbonne Université, Institut Pierre Simon Laplace, 75005 Paris, France
* Correspondence: randel@ucar.edu

Abstract: The eruption of the Hunga Tonga–Hunga Ha'apai (HTHH) volcano on 15 January 2022 injected large amounts of water vapor (H_2O) directly into the stratosphere. While normal background levels of stratospheric H_2O are not detectable in radio occultation (RO) measurements, effects of the HTHH eruption are clearly observed as anomalous refractivity profiles from COSMIC-2, suggesting the possibility of detecting the HTHH H_2O signal. To separate temperature and H_2O effects on refractivity, we use co-located temperature observations from the Microwave Limb Sounder (MLS) to constrain a simplified H_2O retrieval. Our results show enhancements of H_2O up to ~2500–3500 ppmv in the stratosphere (~29–33 km) in the days following the HTHH eruption, with propagating patterns that follow the dispersing volcanic plume. The stratospheric H_2O profiles derived from RO are in reasonable agreement with limited radiosonde observations over Australia. The H_2O profiles during the first few days after the eruption show descent of the plume at a rate of ~−1 km/day, likely due to strong radiative cooling (~−10 K/day) induced by high H_2O concentrations; slower descent (~−200 m/day) is observed over the following week as the plume disperses. The total mass of H_2O injected by HTHH is estimated as 110 ± 14 Tg from measurements in the early plumes during 16–18 January, which equates to approximately 8% of the background global mass of stratospheric H_2O. These RO measurements provide novel quantification of the unprecedented H_2O amounts and the plume evolution during the first week after the HTHH eruption.

Keywords: stratosphere; water vapor; volcanic effects

Citation: Randel, W.J.; Johnston, B.R.; Braun, J.J.; Sokolovskiy, S.; Vömel, H.; Podglajen, A.; Legras, B. Stratospheric Water Vapor from the Hunga Tonga–Hunga Ha'apai Volcanic Eruption Deduced from COSMIC-2 Radio Occultation. *Remote Sens.* **2023**, *15*, 2167. https://doi.org/10.3390/rs15082167

Academic Editor: Manuel Antón

Received: 23 March 2023
Revised: 11 April 2023
Accepted: 15 April 2023
Published: 20 April 2023

1. Introduction

The January 2022 volcanic eruption of Hunga Tonga–Hunga Ha'apai (~20°S, 175°W; hereafter HTHH) was the most explosive eruption in the satellite era, spanning the last four decades. Because HTHH was a submarine eruption, it injected large amounts of water vapor (H_2O) directly into the stratosphere. This behavior is distinctive from other large eruptions from land-locked volcanoes, such as El Chichon in 1982 and Pinatubo in 1991, where enhanced stratospheric H_2O was not observed. Measurements from operational radiosonde balloons over Australia in the first several days after the HTHH eruption show local H_2O mixing ratios greater than 1000 ppmv over altitudes ~25–30 km (the top of the balloon measurements) [1–3], compared with typical stratospheric background H_2O values of 5 ppmv. The isolated balloon measurements showed that the H_2O enhancements occurred in relatively thin ~1–2 km layers. Measurements from the Microwave Limb Sounder (MLS) instrument on the NASA Aura satellite show H_2O perturbations from HTHH that are unprecedented in the satellite data record, in terms of both altitude and magnitude [4]. The MLS data show enhanced H_2O at altitudes up to 53 km immediately

after the eruption (15 January), and maxima between ~25–35 km during the following few days (16–18 January). Maximum H_2O values in these MLS retrievals, which represent vertical averages greater than ~3 km, were ~200–400 ppmv. However, the standard MLS retrievals are not designed for the anomalously high stratospheric H_2O values from HTHH, and many of these early retrievals did not pass the MLS quality screening criteria [4]. The HTHH plume traveled westward and dispersed in the stratosphere, and MLS data show that local H_2O maxima decreased to ~50 ppmv by early February and to ~10–20 ppmv by late March. The MLS retrievals are much better characterized by the lower H_2O values after late January. Anomalously high H_2O from HTHH persists in the stratosphere through boreal winter 2023 and has spread over much of the globe [3,5–7].

The objective of this paper is to quantify the extreme stratospheric H_2O amounts from HTHH in the first week after the eruption using COSMIC-2 (C2) GNSS radio occultation (RO) data. RO measures the bending angle of radio waves propagating through the atmosphere, which is closely related to atmospheric refractivity (N), which, in turn, is dependent on temperature and moisture. Under normal conditions, H_2O makes virtually no contribution to N in the stratosphere and, thus, is not detectable by RO measurements. However, effects from HTHH are clearly observed as anomalous stratospheric bending angle and N profiles from C2 that follow the HTHH plume during the first week after the eruption [3,8,9]. These anomalous N profiles can be associated potentially with both temperature and H_2O effects from the HTHH eruption, and we separate these influences by using independent temperatures from nearby MLS measurements. Reference [3] performed similar calculations using reanalysis temperatures to estimate extreme H_2O amounts in the 15 January HTHH eruption plume. Our analyses focus on the evolution of stratospheric H_2O during the first week after the eruption, as the RO measurements are sensitive only to extreme H_2O amounts. We include comparisons with the limited radiosonde H_2O measurements over Australia (up to ~30 km) to help evaluate the H_2O profiles derived from C2 measurements.

2. Materials and Methods

(a) C2 GNSS-RO observations

By measuring the phase delay of radio waves from GNSS satellites as they slow and bend in Earth's atmosphere, profiles of bending angles and refractivity can be obtained, e.g., [10]. At microwave frequencies in the troposphere and stratosphere, the refractivity varies due to contributions from the dry air and water vapor. Specifically, the atmospheric refractivity N can be related to atmospheric pressure P, temperature T, and water vapor partial pressure e [11]:

$$N = 77.6\left(\frac{P}{T}\right) + 3.73 \times 10^5\left(\frac{e}{T^2}\right) \quad (1)$$

In this study, we obtain level-2 C2 GNSS-RO profiles for January 2022 processed by the COSMIC Data Analysis and Archive Center (CDAAC) at the University Corporation for Atmospheric Research (UCAR). C2 is providing ~6000 profiles/day between ~40°N–40°S. We use the 'atmPrf' product, which provides refractivity and dry temperature (retrieved under the assumption of dry air) from near the surface up to ~60 km; data above 40 km are strongly influenced by climatology; thus, we focus on altitudes 25–35 km in this study. The profiles are quality controlled at CDACC by assigning 'bad' flags on the basis of several metrics, including deviation from the climatology by a specific threshold. A few C2 measurements intersect the early HTHH plume on 15 January and indicate large bending angle or N anomalies [3,6,8,9], but these are flagged as 'bad' retrievals, and most of our analyses focus on observations for 16 January and beyond (we also include a few profiles later in the day on 15 January that passed quality control). The effective vertical resolution of RO soundings varies from ~200 m in the lower troposphere to ~1–2 km in the upper stratosphere (more details below), while the horizontal footprint (horizontal scale represented by a single observation) is ~200 km, e.g., [10].

At CDAAC, the neutral atmosphere profiles are retrieved in the geometric optics approximation above 20 km. In this approximation, the resolution is physically limited by the 1st Fresnel zone F_o [12], which depends on altitude and is approximately 1.4 km at 30 km. At CDAAC, data smoothing is performed using the Savitzky–Golay filter; details can be found in [13]. The half-width of the filter response function used for the standard processing is $1.1F_0$~1.5 km at 30 km. Specifically for this study, we investigated the possibility of modifying the filtering in order to better resolve those N structures in the stratosphere induced by HTHH eruption. By modeling and testing we found that reducing the half-width of the response function by one-half, to 0.75 km at 30 km, results in improvement of the vertical resolution at 30 km, without substantial increase of the effect of observational noise (mainly from the ionosphere), while further reduction increases the noise and creates artifacts in the profiles. Thus, C2 RO data used in this study were processed with twice increased vertical resolution compared with the standard retrieval.

(b) MLS temperatures

MLS temperatures are retrieved using measured limb emission from atmospheric oxygen (O_2), and these data are not strongly influenced by the HTHH eruption. We use MLS temperature profiles based on the v4.2 retrieval [14]. MLS provides global sampling with approximately 3500 measurements per day. Temperature retrievals are provided on standard pressure levels; data extend from 261 hPa (~9 km) to greater than 1 hPa (~48 km), with an effective vertical resolution of 3–4 km over the main region of interest here (~30 km).

(c) Radiosondes

We include comparisons with radiosonde measurements of stratospheric H_2O during the first few days after the HTHH eruption. These data are discussed in detail in [2] and are based on measurements from the operational upper air network using the Vaisala RS41 radiosonde. These data can detect the large stratospheric H_2O from HTHH, and provide measurements up to ~30 km (depending on the balloon burst altitude of individual flights) with vertical resolution of ~100 m.

3. Results

3.1. RO Sensitivity to Stratospheric H_2O

N decreases with altitude in the troposphere and stratosphere, and the H_2O term in (1) contributes little to N above the middle troposphere, where $H_2O < 100$ ppmv (e.g., [15]). Sensitivity tests based on (1) can determine the magnitude of GNSS-RO refractivity variations expected from isolated H_2O and temperature anomalies in the stratosphere. The sensitivity of N to isolated large stratospheric H_2O perturbations (1000 and 1500 ppmv anomalies at 30 km) is illustrated in Figure 1, showing positive N anomalies of ~2% and 3%, respectively, compared with an unperturbed background. While these are relatively small fractional N anomalies, they are not small compared with the observed N standard deviation in the stratosphere measured by C2, with typical values of 1% background levels (as shown in Figure 1; these were calculated from the pre-volcanic C2 measurements during 1–14 January in the vicinity of HTHH). Hence, an N anomaly due to a 1500 ppmv increase in H_2O is comparable to a (rare) positive 3-sigma C2 noise event. Figure 1 also shows the N anomaly associated with a local −8 K temperature perturbation at 30 km, which is similar (~3.5%) to the effect of 1500 ppmv H_2O. These calculations suggest that C2 RO measurements may be able to detect a large stratospheric H_2O perturbation on the order of 1000 ppmv or larger but that similar N signals can arise from large negative temperature anomalies.

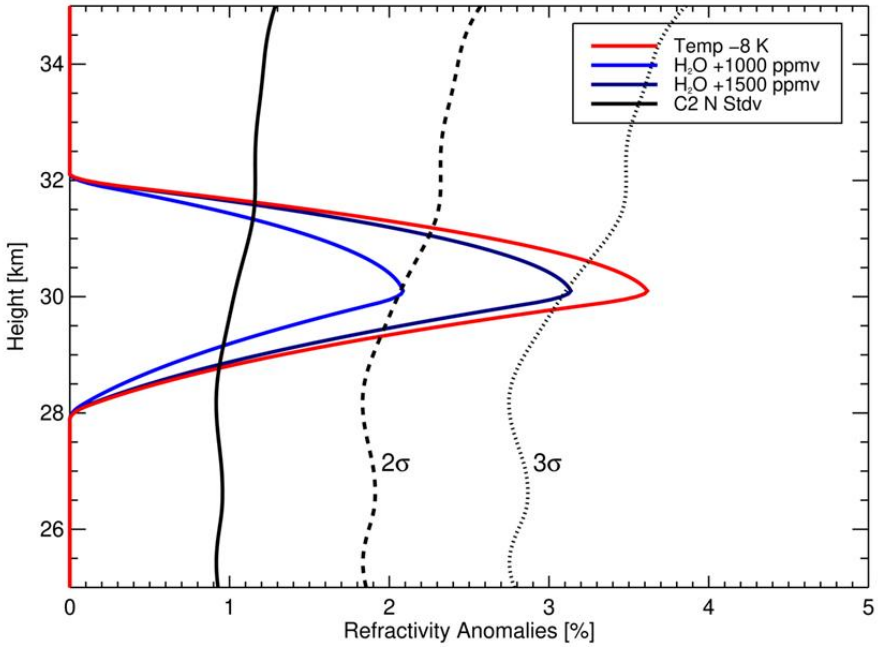

Figure 1. Vertical profiles of refractivity (*N*) anomalies associated with localized 1000 and 1500 ppmv H_2O perturbations at 30 km and for a −8 K temperature perturbation. Results are expressed in terms of percentage anomalies with respect to a standard background *N* profile. The solid black line shows the observed standard deviation (sigma) for C2 *N* measurements based on non-volcanic conditions in the vicinity of HTHH, and the dashed and dotted lines show 2-sigma and 3-sigma values, respectively.

3.2. C2 HTHH Refractivity Observations and H_2O Retrievals

On the basis of the sensitivity calculations shown in Figure 1, our analyses search for positive *N* anomalies in C2 data that are larger than 3-sigma. Anomalies are calculated as percentage differences from the pre-volcanic background 1–14 January average. Figure 2 shows the C2 daily sampling density in the region of the HTHH eruption on 16–18 January (grey dots) along with the locations of local *N* anomalies with maximum values greater than 3-sigma over altitudes 25–35 km (colored symbols). The stratospheric plume from HTHH moved westward in the background stratospheric easterly winds (e.g., [1–4]), and the positive *N* anomalies >3-sigma in Figure 2 track the plume movement downstream from the 15 January eruption. The altitudes of the *N* anomaly maxima for these days generally range from 27 to 33 km. For comparison, Figure 2 includes corresponding maps of sulfur dioxide (SO_2) in the HTHH plume, as observed by satellite [16], showing westward movement and dispersion of the plume similar to that inferred from the C2 *N* anomalies.

Examples of the vertical profiles of *N* anomalies for the cases identified on 16 January (Figure 2a) are shown in Figure 3a. As selected, each of the profiles has a maximum *N* anomaly greater than 3%, with several local maxima greater than 6%, and the observed profiles peak over altitudes ~29–33 km. The vertical thickness of the *N* anomaly profiles is, on average, ~2 km.

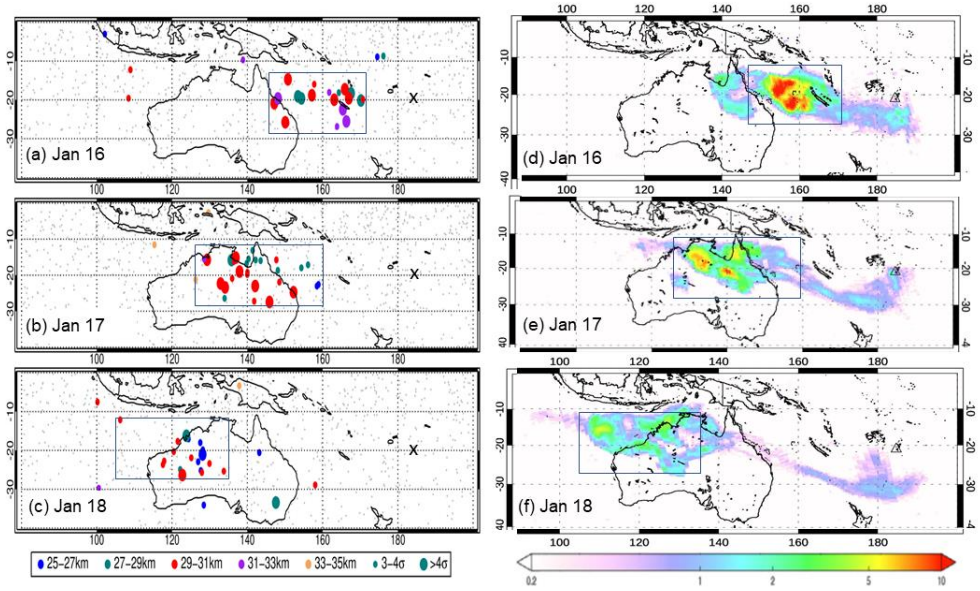

Figure 2. Left panels (**a**–**c**) show the C2 sounding locations (grey dots) in the region of the HTHH eruption on 16–18 January. Colored symbols indicate locations with positive N anomalies over altitudes 25–35 km exceeding 3-sigma background values, with color and size denoting the altitude and magnitude of the maximum N anomaly. Right panels (**d**–**f**) show satellite SO_2 measurements denoting the HTHH plume locations on these same days, from [16]. The color scale denotes column SO_2 amounts in Dobson Units (DU). Boxes in each panel denote the approximate plume areas used to estimate the H_2O mass.

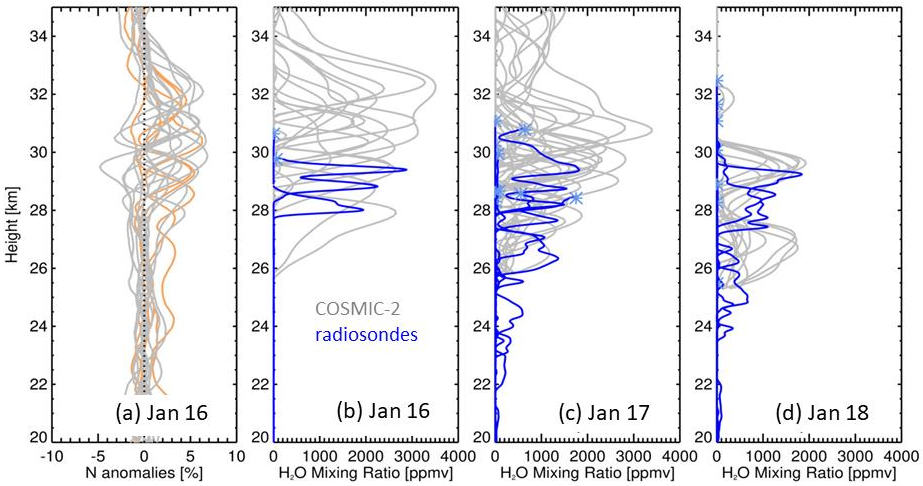

Figure 3. (**a**) Vertical profiles of refractivity (N) anomalies for cases selected on 16 January (colored symbols in Figure 2a). The orange lines indicate profiles with multiple maxima in altitude that are not used for H_2O retrievals. (**b**–**d**) Vertical profiles of C2-derived H_2O mixing ratios (grey lines) for the cases selected during 16–18 January (colored symbols in Figure 2a–c), excluding cases with multiple N maxima. The blue lines in (**b**–**d**) show radiosonde H_2O measurements over Australia during these days from [2]. Note that the radiosonde data extend only upwards to the balloon-burst altitude near ~30 km; the highest measurements in each profile are indicated by the blue asterisks.

Details of retrieving H_2O from C2 N measurements combined with ancillary temperature profiles from MLS are described in the Appendix A. Our results use the local retrieval based on Equation (1), incorporating C2 N observations with the nearest co-located MLS temperature profile (within 600 km and 6 h), and we use dry pressure (P_{dry}) from the C2 atmPrf files. We then solve Equation (1) for water vapor pressure e and convert to H_2O mixing ratio. As discussed in the Appendix A, this local retrieval will underestimate H_2O

amounts compared with a more accurate non-local retrieval, but the underestimate is small (~10%) for narrow ~2 km thick H_2O layers, as is typical for HTHH. Our local H_2O retrievals also truncate at the bottom of the layer where the retrieved H_2O becomes negative, which results in a slight underestimation of the column amount. There are somewhat larger errors associated with multiple H_2O layers (Figure A2), and we simply omit a handful of profiles that exhibit multiple layers (mostly on 16 January, indicated by the orange curves in Figure 3a).

Figure 3b shows the derived H_2O profiles on 16 January, with maximum H_2O values of ~2500–3500 ppmv over altitudes ~29–33 km; the altitude maxima for H_2O approximately match the *N* anomaly maxima in Figure 3a. We note that these large H_2O amounts are below ice saturation with respect to the background stratospheric temperatures that increase with height (e.g., [1–3]). Figure 3c,d show derived H_2O profile results for the following days, showing a decrease in the maximum H_2O amounts to ~2000–3000 ppmv on 17 January and ~1800 ppmv on 18 January. The measured altitudes of the H_2O maxima also systematically decrease between 16–18 January.

While the HTHH plume was over Australia during 16–18 January, enhanced stratospheric H_2O was observed by operational radiosonde balloons [1–3]. H_2O profiles from these radiosonde data are shown in Figure 3 overlain on the RO retrievals. Note that the top of the radiosonde measurements is near 30 km (depending on the individual balloon flights), so that direct comparisons with RO calculations focus on altitudes below 30 km. In addition, the radiosonde profiles are not explicitly co-located with the C2 profiles but are intended to be representative of approximate H_2O magnitudes and altitudes in this region. The radiosonde-C2 comparisons in Figure 3b–d show reasonable agreement over ~26–30 km in terms of H_2O magnitude during these days, e.g., ~2000–3000 ppmv on 16 January. This agreement enhances confidence in the C2 H_2O retrievals, at least for the extreme maxima immediately following the eruption.

We also investigated several C2 measurements that intersected the HTHH plume early after the eruption on 15 January, and the associated *N* anomalies and retrieved H_2O amounts are shown in Figure 4. The results show large positive *N* anomalies (~10–25%) and extreme H_2O values (~4000–10,000 ppmv) over altitudes 30–40 km. However, these retrieved *N* profiles are mostly classified as 'bad', and the reason is not simply understood because there are numerous potential causes. While we are less confident in these retrievals, the vertical structure is reasonable, and the large H_2O values in Figure 4 are still below ice saturation and, thus, may represent actual geophysical structure, as noted in [3].

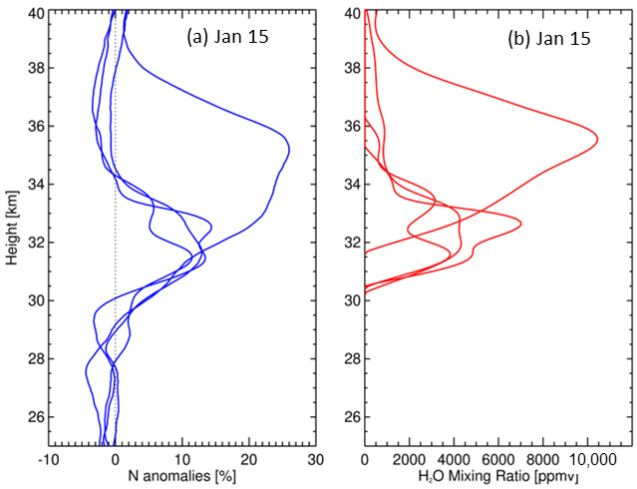

Figure 4. Vertical profiles of (**a**) refractivity anomaly and (**b**) derived H_2O mixing ratios for C2 observations within the HTHH plume on 15 January. Most of these *N* profiles are associated with a 'bad' flag in the retrieval, although the structures are reasonable and may be consistent with actual geophysical information.

Analyses of the MLS temperatures show that there are not systematic temperature anomalies associated with the identified C2 *N* anomalies for the volcanic plume events (Figure 5), so that the stratospheric RO *N* anomalies arise primarily from enhanced H_2O. This statement is qualified by the lower vertical resolution of MLS temperatures (~4 km) compared with C2 retrievals (~1–2 km), in addition to imprecise co-locations of the MLS and C2 data. In contrast to the lack of temperature anomalies in the MLS data, temperatures derived from the C2 dry retrieval (atmPrf, neglecting the H_2O term in Equation (1)) show negative temperature anomalies up to −20 K (Figure 5). These are likely spurious results related to the large positive *N* anomalies when not accounting for H_2O effects. As a note, we have also examined co-located temperatures from ERA5 reanalysis [17] and find small systematic temperature anomalies for the co-locations, similar to the MLS results in Figure 5.

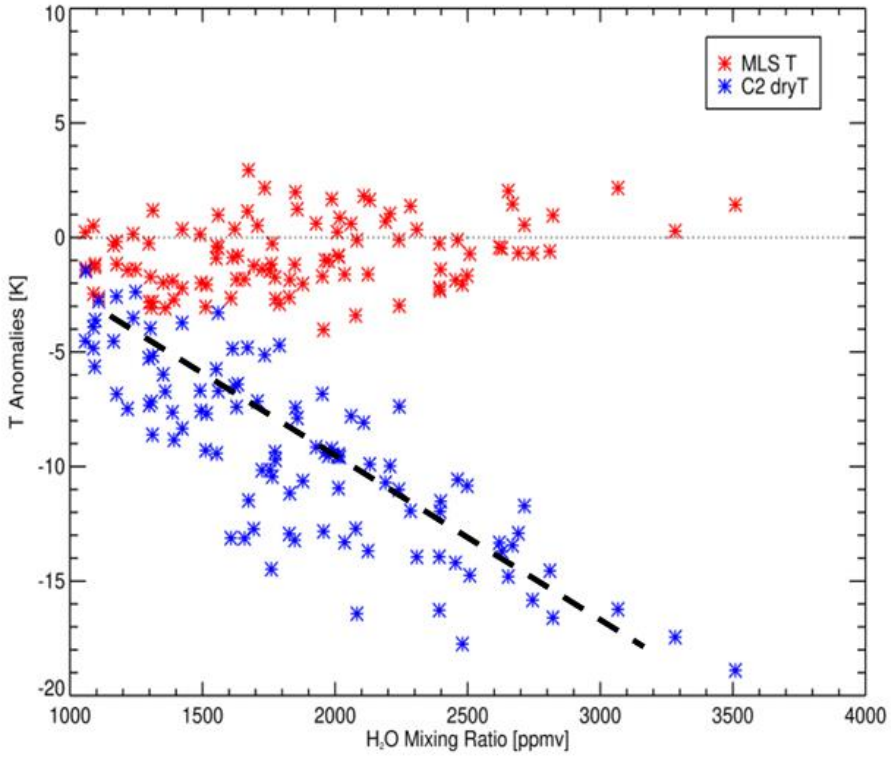

Figure 5. Red symbols show MLS temperature anomalies as a function of retrieved H_2O amount in the HTHH plume over 16–18 January (the same profiles as identified in Figure 3). Temperature anomalies are calculated at the altitude of the maximum retrieved H_2O in each profile. Blue symbols show the corresponding dry temperature anomalies calculated in the C2 dry retrievals (atmPrf). Black dashed line corresponds to a slope of (−8 K/1600 ppmv), consistent with the T-H_2O sensitivity results shown in Figure 1.

Regular westward propagation of the HTHH H_2O plume is detected by RO measurements over the first week after the eruption, as shown in Figure 6, selected for profiles with derived H_2O values > 1000 ppmv over 25–35 km. This behavior is in good agreement with the MLS H_2O retrievals shown in [4], which also demonstrated consistency with the background stratospheric easterly winds. Figure 6 also shows that while the enhanced H_2O values from HTHH clearly stand out, there are numerous additional events that are not coincident with the plume, and these likely represent noise in the C2 *N* profiles.

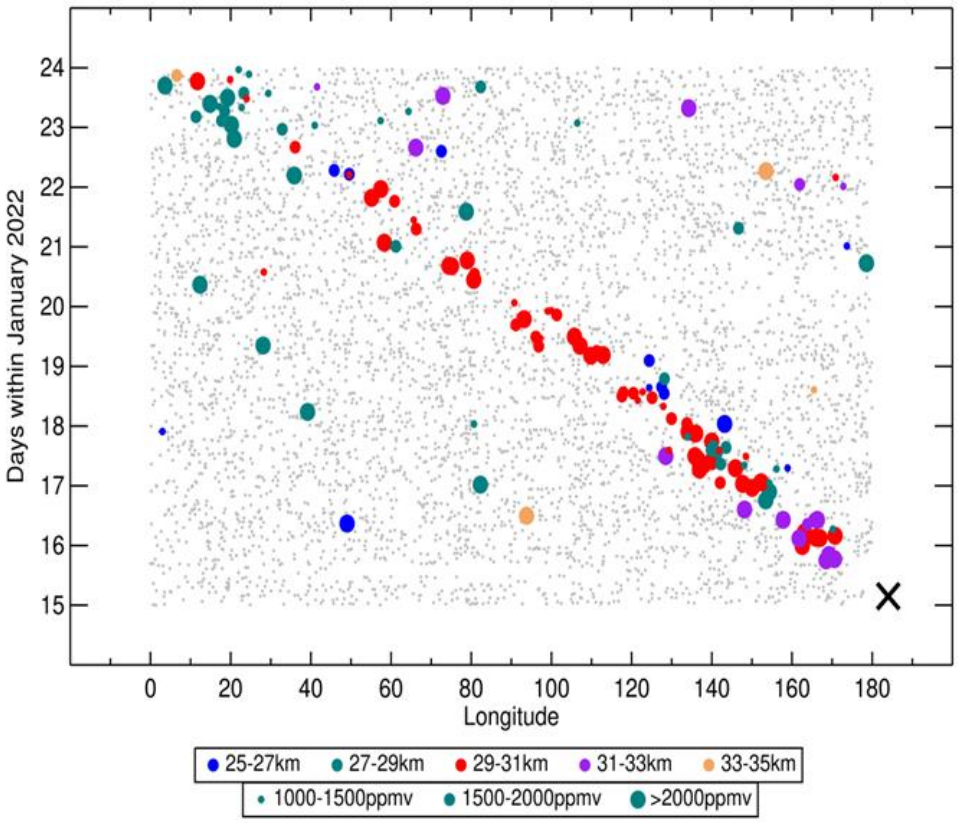

Figure 6. Longitude vs. time diagram showing locations of H_2O profiles with maximum values >1000 ppmv over 25–35 km, over the domain 10–30°S, for the first week following the HTHH eruption (noted by the 'X' on 15 January). The colors and symbols denote the altitudes and concentrations of the H_2O maxima. The grey dots indicate all of the C2 measurement locations.

For the H_2O profiles identified in the HTHH plume (i.e., following the locus of westward propagating points in Figure 6), Figure 7 shows the corresponding derived plume height and thickness and the corresponding maximum H_2O values. Plume thickness is estimated as the altitudes over which H_2O exceeds 25% of the maximum value in each respective profile. Results show highest H_2O concentrations (up to ~3500 ppmv) and highest altitudes (~29–33 km) immediately after the eruption on 16 January. Maximum H_2O concentrations decrease, and the plume heights descend by ~2 km over the first two days, as seen in Figure 3. Maximum H_2O values are ~1000–2500 ppmv after 18 January, and some isolated larger H_2O maxima over 20–22 January could possibly be related to localized plume maxima identified in [6]. The general decreases in H_2O concentration and altitude are consistent with observations from radiosonde data [2,3] and MLS [4,7] following the eruption. The descent rate for the period 18–23 January in Figure 7a is approximately 200 m/day, which is consistent with values estimated from radiosondes over the first zonal circumnavigation of the plume [3]. We find less coherent variability in derived C2 H_2O amounts after ~24 January. Given the RO H_2O sensitivity inferred from Figure 1, together with observed C2 noise levels, we expect that C2 will lose sensitivity to stratospheric H_2O amounts below ~1000 ppmv (which corresponds to positive N anomalies ~2-sigma).

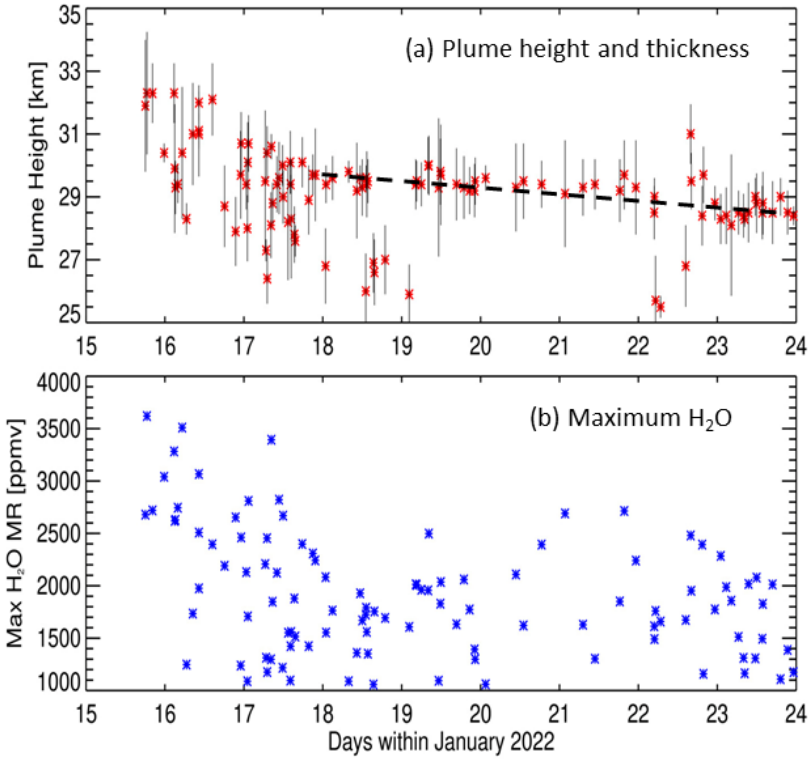

Figure 7. Time series of (**a**) plume height and thickness, and (**b**) H_2O maximum concentration for C2 H_2O retrievals in the HTHH plume, selected as the westward propagating maxima in Figure 6. Vertical lines in (**a**) denote the plume thickness, showing altitudes where H_2O is greater than 25% of the maximum value in each profile. The black dashed line in (**a**) indicates a slope of −200 m/day during 18–23 January.

3.3. Mass of H_2O in the Early HTHH Plume

We calculate the mass of H_2O in the early HTHH plumes during 16–18 January by estimating the approximate area of the plumes and then integrating the derived H_2O profiles for all of the RO measurements within the plume areas. The estimated plume areas are shown in Figure 2, defined simply as latitude–longitude boxes containing enhanced *N* anomalies for each day. These boxes agree well with the approximate plume areas defined by maximum SO_2 amounts (Figure 2d–f), and the box on 18 January is selected with this agreement in mind. We calculate the vertically integrated H_2O (over 25–35 km) using all of the profiles within the boxes (not just the extreme N > 3-sigma profiles), and this accounts for heterogeneity of the plume structure. Multiplying the plume areas by the integrated H_2O profile amounts determines the H_2O mass within the plume volumes. Results of these calculations return values of 98 ± 11, 103 ± 14 and 102 ± 14 Tg (2-sigma uncertainties) on the three days of 16–18 January. Uncertainties in these estimates are derived by repeating the calculations numerous times but including random Gaussian-distributed ±1% variations to the individual *N* and T profiles, consistent with background noise in the C2 *N* measurements and uncertainties in the ancillary MLS temperatures. We note that the estimates for these three days are remarkably consistent (~100 Tg), given the evolving horizontal (Figure 2) and vertical (Figure 3) structure of the plumes over these days. Including the systematic underestimation of H_2O amounts by the local retrieval by ~10% provides an average value with uncertainties of 110 ± 14 Tg for the total mass, which equates to approximately 8% of the background mass of stratospheric water vapor. This value is consistent with the MLS v5 results [3] and somewhat less than those of MLS v4 [4]. Reference [3] estimated the H_2O mass from two individual RO measurements within the HTHH eruption umbrella on 15 January, giving a broad range of 70–150 Tg, which overlaps our results for 16–18 January.

4. Discussion

C2 data demonstrate that RO measurements are sensitive to the extremely large stratospheric H_2O perturbations during the first week following the HTHH eruption. This is tied to the large observed refractivity anomalies associated with the HTHH plume, combined with the low stratospheric background noise in the C2 measurements (with standard deviations of ~1% background values). Sensitivity calculations (Figure 1) suggest that stratospheric H_2O anomalies of ~1000–1500 ppmv or larger should be detectable in C2 refractivity measurements, equivalent to 2-sigma and 3-sigma noise levels, respectively. N anomalies for 1500 ppmv have similar magnitude to a localized -8 K temperature perturbation.

To separate H_2O and temperature effects on N, we used independent temperature observations from the MLS satellite. This has some limitations in terms of different vertical sensitivities and imperfect co-locations between C2 and MLS measurements but is a necessary step to separate H_2O and temperature influences on N. Comparison of MLS temperature anomalies vs. derived H_2O amount (Figure 5) suggests small systematic temperature anomalies for the H_2O plume during the first week after the eruption so that the C2 N anomalies are due primarily to H_2O influence. In contrast, C2 dry temperature retrievals (atmPrf) for the anomalous HTHH profiles analyzed here show large negative temperature anomalies (up to -20 K in Figure 5), which are believed to represent mainly the response of dry temperature to H_2O. We note that [2] identified small systematic temperature anomalies (~$-$2K) associated with enhanced H_2O in the radiosonde measurements after 29 January, possibly linked with radiative cooling from enhanced H_2O [1], but such patterns are not detected in MLS results (or ERA5 reanalysis) during the first week after the eruption. Larger systematic cold temperature anomalies (zonal means greater than 5 K) are observed in the months following HTHH, likely as a radiative and dynamical response to the anomalous H_2O and aerosols [18].

Our simple H_2O retrieval shows maximum values of ~2500–3500 ppmv during the first few days following the eruption, over altitudes ~29–33 km. The H_2O magnitudes from the C2 retrieval are in reasonable agreement with radiosonde measurements over Australia, which cover altitudes up to ~30 km. MLS H_2O retrievals show smaller maximum values (~200–400 ppmv) over these days, but the MLS vertical sensitivity represents broader vertical layers (~3–4 km thick) that can underestimate the peak concentration and overestimate the vertical extent for narrow layers. C2 measurements show a relatively rapid descent (~$-$1 km/day) of the plume over the first two days when H_2O concentrations are highest, and slower descent (~200 m/day) during the following week. Radiative cooling from the early H_2O enhancements [1] produces values of ~$-$10 K/day, which equate to ~$-$30 K/day in potential temperature or ~$-$1 km/day over altitudes near 30 km, which is approximately consistent with the C2 observations. Cooling and descent rates drop rapidly with H_2O dilution, as observed during the following week.

Combining the horizontal extent of the H_2O plumes observed by RO with the derived H_2O profiles provides a total mass of ~110 $\pm$ 14 Tg for the early plumes during 16–18 January. This estimate from RO data is in approximate agreement with results using MLS v5 retrievals of 119 $\pm$ 6 Tg [3], while MLS v4 data provide higher values of 137–146 $\pm$ 8 Tg [3–5]. Total HTHH H_2O mass estimates from radiosondes [2] provide values of 50–93 Tg but are limited by the vertical extent of the balloon measurements (~30 km). We note that while there are no observations of an increase in stratospheric H_2O after the Pinatubo eruption in 1991, reference [19] calculated 37.5 Tg injection of water vapor to the stratosphere in an idealized model. Combining the H_2O sensitivity of RO with C2 background noise levels suggests that the C2 measurements are less sensitive to H_2O amounts below ~1000 ppmv (equivalent to 2-sigma noise levels) so that C2 measurements are most useful for the large H_2O amounts in the first week after HTHH. Both radiosonde [2] and MLS data [3,4] show that the HTHH plume disperses over time, with H_2O values <100 ppmv several weeks after the eruption. These smaller values, while highly anomalous and long-lasting in the stratosphere, are not retrievable from RO measurements.

Author Contributions: Conceptualization, A.P., B.L. and W.J.R.; methodology, W.J.R., B.R.J. and S.S.; software, B.R.J.; investigation, W.J.R., B.R.J., J.J.B., S.S., H.V., A.P. and B.L.; writing—original draft preparation, W.J.R.; writing—review and editing, W.J.R., B.R.J., J.J.B., S.S., H.V., A.P. and B.L. All authors have read and agreed to the published version of the manuscript.

Funding: The National Center for Atmospheric Research is sponsored by the U.S. National Science Foundation, and work in COSMIC is supported under the NSF-NASA Cooperative Agreement Grant 1522830 and NOAA NSCP Coop award NA21OAR4310383.

Data Availability Statement: The specially processed COSMIC-2 data are archived at the COSMIC Data Analysis and Archive Center (CDAAC) website https://data.cosmic.ucar.edu/gnss-ro/publications/hthh2022/ (accessed on 20 March 2022). MLS temperatures were obtained from the NASA website https://doi.org/10.5067/Aura/MLS/DATA2021 (accessed on 15 May 2022). ERA5 reanalysis temperatures were obtained through the Copernicus Climate Data Store: https://cds.climate.copernicus.eu/cdsapp#!/dataset/reanalysis-era5-pressure-levels?tab=overview (accessed on 10 June 2022). The radiosonde H_2O profiles were obtained as described in Vömel et al. (2022), with data at https://doi.org/10.5065/p328-z959 (accessed on 25 July 2022).

Acknowledgments: We thank the MLS group at the NASA Jet Propulsion Laboratory for helpful discussions, and we thank Rick Anthes for review and comments on the manuscript. Two anonymous reviewers provided constructive comments that substantially improved the paper.

Conflicts of Interest: The authors declare no conflict of interest.

Appendix A. Retrieval of Water Vapor from Radio Occultation Refractivity and Ancillary Temperature Data

Here, we compare two water vapor retrieval methods using RO refractivity and temperature obtained from ancillary data. As shown in Section 2, refractivity N is related to the following atmospheric parameters:

$$N = c_1 \frac{P}{T} + c_2 \frac{e}{T^2} \tag{A1}$$

where P is total air pressure, e is partial pressure of water vapor, T is temperature, $c_1 = 77.6\ \frac{K}{mb}$, and $c_2 = 3.73 \times 10^5\ \frac{K^2}{mb}$. The atmospheric parameters satisfy the hydrostatic equation:

$$\frac{dP}{dz} = -g\rho \tag{A2}$$

where z is height, g is gravitational acceleration, and ρ is density; along with the equation of state of moist air:

$$P = R_d \rho T_v \tag{A3}$$

where $R_d = 287\ \frac{J}{kgK}$ is the gas constant for dry air, and the effect of water vapor is taken into account by virtual temperature:

$$T_v = T / \left(1 - c_3 \frac{e}{P}\right) \tag{A4}$$

where $c_3 = 1 - \frac{m_w}{m_d} = 0.378$; and m_w and m_d are the molecular weights of water vapor and dry air, respectively.

If the air is dry, $e = 0$ and $T_v = T$, and Equations (A1)–(A3) are sufficient to solve for P and T from N by numerical integration. This solution is routinely applied in the standard RO processing and is denoted P_{dry} and T_{dry}. However, P_{dry} and T_{dry} differ from the true P and T when $e \neq 0$. Thus, to solve for e, additional information (typically temperature obtained from ancillary data T_{anc}) is needed.

A simple approach to retrieve water vapor is based on neglecting the difference between P and P_{dry}, which is approximately true for thin layers of water vapor. This retrieval, hereafter called "local", is obtained directly from Equation (A1):

$$e_1(z) = \frac{T_{anc}^2(z)}{c_2}(N(z) - c_1 P_{dry}(z) T_{anc}(z))$$

Alternatively, Equations (A1)–(A4) can be solved for $e(z)$ for a given $N(z)$ and $T_{anc}(z)$ by numerical integration without any approximations. This retrieval, hereafter called "non-local", is denoted by $e_2(z)$. Below, we show examples of $e_1(z)$ errors related to the vertical structure of water vapor and examples of both $e_1(z)$ and $e_2(z)$ errors related to uncertainties of $T_{anc}(z)$. Instead of e, we present results in terms of water vapor mixing ratio (in ppmv):

$$r = 10^6 \times c_4 \frac{e}{P - e}, \text{ where } c_4 = \frac{m_w}{m_d} = 0.622$$

Figure A1 shows models of a single water vapor layer $e(z) = \frac{e_0\left[1+\frac{\cos 2\pi(z-z_0)}{\Delta z}\right]}{2}$ for $z_0 = 30$ km and $\Delta z = 2, 4, 6, 8$ km. The models $e(z)$, which include, for simplicity, a constant temperature $T(z) = 250$ K, were used for numerical integration of Equations (A2)–(A4) to obtain $P(z)$. Next, $N(z)$ was obtained from Equation (A1). Thus, the defined $T(z)$ and obtained $N(z)$ were used as initial conditions for local and non-local retrievals $e_1(z)$ and $e_2(z)$. Figure A1 shows that local retrievals $e_1(z)$ are negatively biased, and the bias is larger for larger Δz (thicker H_2O layers). For $\Delta z = 2$ km, the local retrieval error at the center of the layer is <10%. The height below which $e_1(z) < 0$ may be considered ad hoc as a lower height of the local retrieval for a single layer, and the derived layer thickness for the local retrieval also underestimates the true values. Non-local retrievals $e_2(z)$ are indiscernible from the model $e(z)$.

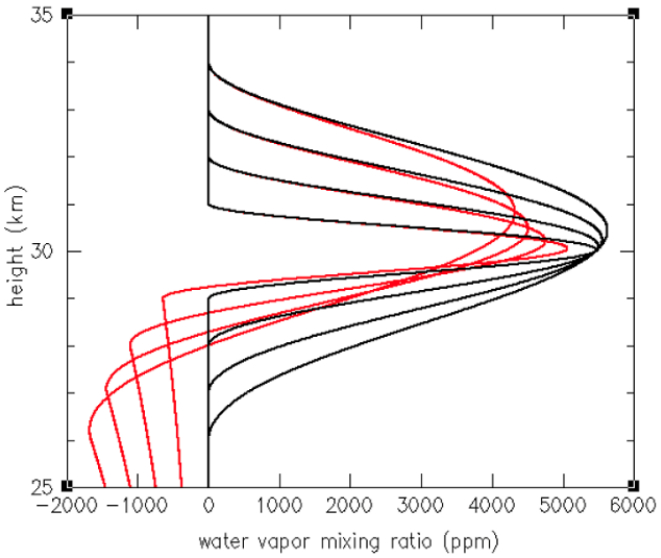

Figure A1. Idealized water vapor profiles e(z) (black lines), along with profiles derived using the local retrieval (red) and nonlocal retrieval (overlapping black lines) for different water vapor layer thicknesses ($\Delta z = 2, 4, 6$ and 8 km).

Figure A2 shows the model of multiple layers with $\Delta z = 2$ km, and these layers decrease in concentration at lower altitudes because of the conversion from partial pressure to mixing ratio. Figure A2 shows that the local retrieval $e_1(z)$ has a negative bias increasing downward with each successive layer, while the non-local retrieval $e_2(z)$ is again indiscernible from the model $e(z)$.

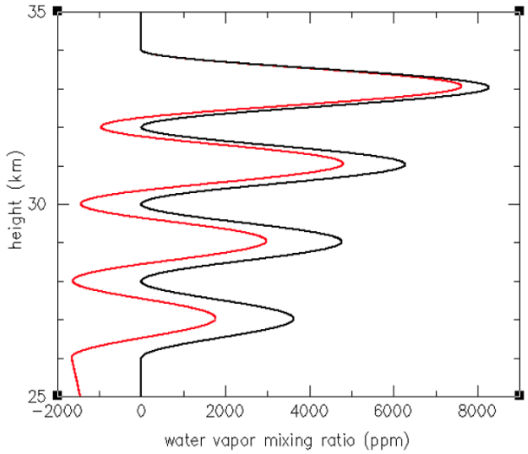

Figure A2. Water vapor profiles using the non-local retrieval (black) and local retrieval (red) when multiple layers of water vapor are present. The non-local retrievals $e_2(z)$ directly overlap the specified idealized layers.

Examples in Figures A1 and A2 may suggest that the non-local retrieval $e_2(z)$ should always be used. However, temperature $T_{anc}(z)$ obtained from an ancillary observation generally has an uncertainty composed of the measurement error and representativeness difference with RO. Here, we test local and non-local retrievals by using $T_{anc}(z)$, which differs from $T(z)$.

Figure A3 shows the model $e(z)$, $e_1(z)$, and $e_2(z)$ obtained by using model $T(z) = 250$ K. Green and blue lines show $e_1(z)$ and $e_2(z)$, respectively, obtained by using $T_{anc}(z)$, which differs from $T(z)$ by $\pm 1\%$. In this case, the error of the nonlocal retrieval $e_2(z)$ is larger than the disturbance of $e_1(z)$. Furthermore, $e_2(z)$ results in positive errors below the single layer, which may not allow for ad hoc determination of the lower height of the layer by $e = 0$, which is still possible with $e_1(z)$. This explains our choice of local retrieval in this study since most N anomaly profiles indicate the existence of a single water vapor layer at a height of approximately ~30 km. In such cases, the local retrieval is limited by the height where e becomes negative. Retrieval of a water vapor profile below the bottom of the upper layer of water vapor is an ill-conditioned problem (because of the errors of local retrieval and the sensitivity of the non-local retrieval to ancillary temperature errors) and is not considered in this study.

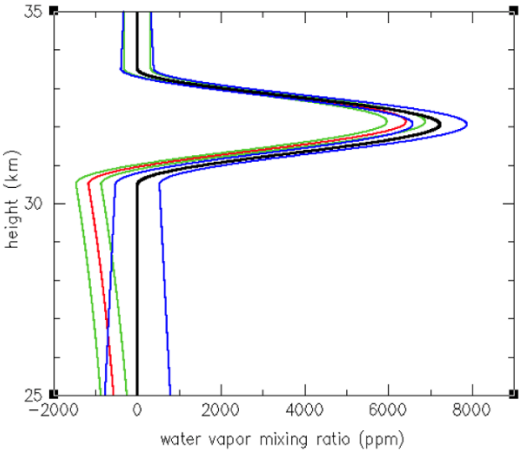

Figure A3. Water vapor profiles using the non-local retrieval (black) and local retrieval (red). Water vapor profiles retrieved with $T_{anc}(z)$ differing from $T(z)$ by $\pm 1\%$ using the non-local retrieval (blue) and local retrieval (green).

References

1. Sellitto, P.; Podglajen, A.; Belhadji, R.; Boichu, M.; Carboni, E.; Cuesta, J.; Duchamp, C.; Kloss, C.; Siddans, R.; Bègue, N.; et al. The unexpected radiative impact of the Hunga Tonga eruption of 15th January 2022. *Commun. Earth Environ.* **2022**, *3*, 288. [CrossRef]
2. Vömel, H.; Evan, S.; Tully, M. Water vapor injection into the stratosphere by Hunga Tonga-Hunga Ha'apai. *Science* **2022**, *377*, 1444–1447. [CrossRef] [PubMed]
3. Khaykin, S.; Podglajen, A.; Ploeger, F.; Grooß, J.-U.; Tence, F.; Bekki, S.; Khlopenkov, K.; Bedka, K.; Rieger, L.; Baron, A.; et al. Global perturbation of stratospheric water and aerosol burden by Hunga eruption. *Commun. Earth Environ.* **2022**, *3*, 316. [CrossRef]
4. Millán, L.; Santee, M.L.; Lambert, A.; Livesey, N.J.; Werner, F.; Schwartz, M.J.; Pumphrey, H.C.; Manney, G.L.; Wang, Y.; Su, H.; et al. The Hunga Tonga-Hunga Ha'apai Hydration of the Stratosphere. *Geophys. Res. Lett.* **2022**, *49*, e2022GL099381. [CrossRef] [PubMed]
5. Xu, J.; Li, D.; Bai, Z.; Tao, M.; Bian, J. Large Amounts of Water Vapor Were Injected into the Stratosphere by the Hunga Tonga–Hunga Ha'apai Volcano Eruption. *Atmosphere* **2022**, *13*, 912. [CrossRef]
6. Legras, B.; Duchamp, C.; Sellitto, P.; Podglajen, A.; Carboni, E.; Siddans, R.; Grooß, J.-U.; Khaykin, S.; Ploeger, F. The evolution and dynamics of the Hunga Tonga–Hunga Ha'apai sulfate aerosol plume in the stratosphere. *Atmos. Chem. Phys.* **2022**, *22*, 14957–14970. [CrossRef]
7. Schoeberl, M.R.; Wang, Y.; Ueyama, R.; Taha, G.; Jensen, E.; Yu, W. Analysis and impact of the Hunga Tonga-Hunga Ha'apai stratospheric water vapor plume. *Geophys. Res. Lett.* **2022**, *49*, e2022GL100248. [CrossRef]
8. Carr, J.L.; Horváth, Á.; Wu, D.L.; Friberg, M.D. Stereo Plume Height and Motion Retrievals for the Record-Setting Hunga Tonga-Hunga Ha'apai Eruption of 15 January 2022. *Geophys. Res. Lett.* **2022**, *49*, e2022GL098131. [CrossRef]
9. Ravindra Babu, S.; Lin, N.-H. Extreme Heights of 15 January 2022 Tonga Volcanic Plume and Its Initial Evolution Inferred from COSMIC-2 RO Measurements. *Atmosphere* **2023**, *14*, 121. [CrossRef]
10. Anthes, R.A.; Bernhardt, P.A.; Chen, Y.; Cucurull, L.; Dymond, K.F.; Ector, D.; Healy, S.B.; Ho, S.-P.; Hunt, D.C.; Kuo, Y.-H.; et al. The COSMIC/FORMOSAT-3 Mission: Early Results. *Bull. Am. Meteorol. Soc.* **2008**, *89*, 313–333. [CrossRef]
11. Smith, E.K.; Weintraub, S. The Constants in the Equation for Atmospheric Refractive Index at Radio Frequencies. *Proc. IRE* **1953**, *41*, 1035–1037. [CrossRef]
12. Kursinski, E.R.; Hajj, G.A.; Schofield, J.T.; Linfield, R.P.; Hardy, K.R. Observing Earth's atmosphere with radio occultation measurements using the Global Positioning System. *J. Geophys. Res.* **1997**, *102*, 23429–23465. [CrossRef]
13. Zeng, Z.; Sokolovskiy, S.; Schreiner, W.S.; Hunt, D. Representation of Vertical Atmospheric Structures by Radio Occultation Observations in the Upper Troposphere and Lower Stratosphere: Comparison to High Resolution Radiosonde Profiles. *J. Atmos. Ocean. Technol.* **2019**, *36*, 655–670. [CrossRef]
14. Livesey, N.J. Aura Microwave Limb Sounder (MLS) Version 4.2x Level 2 and 3 Data Quality and Description Document. 2018. Available online: http://mls.jpl.nasa.gov/ (accessed on 20 November 2018).
15. Johnston, B.R.; Randel, W.J.; Braun, J.J. Interannual Variability of Tropospheric Moisture and Temperature and Relationships to ENSO using COSMIC-1 GNSS-RO Retrievals. *J. Clim.* **2022**, *35*, 3509–3525. [CrossRef]
16. Carn, S.A.; Krotkov, N.A.; Fisher, B.L.; Li, C. Out of the blue: Volcanic SO_2 emissions during the 2021–2022 eruptions of Hunga Tonga—Hunga Ha'apai (Tonga). *Front. Earth Sci.* **2022**, *10*, 976962. [CrossRef]
17. Hersbach, H.; Bell, B.; Berrisford, P.; Hirahara, S.; Horányi, A.; Muñoz-Sabater, J.; Nicolas, J.; Peubey, C.; Radu, R.; Schepers, D.; et al. The ERA5 global reanalysis. *Quart. J. R. Meteor. Soc.* **2020**, *146*, 1999–2049. [CrossRef]
18. Wang, X.; Randel, W.; Zhu, Y.; Tilmes, S.; Starr, J.; Yu, W.; Garcia, R.; Toon, B.; Park, M.; Kinnison, D.; et al. Stratospheric climate anomalies and ozone loss caused by the Hunga Tonga volcanic eruption. *Authorea* 2022, *preprint*. [CrossRef]
19. Pitari, G.; Mancini, E. Short-term climatic impact of the 1991 volcanic eruption of Mt. Pinatubo and effects on atmospheric tracers. *Nat. Hazards Earth Syst. Sci.* **2002**, *2*, 91–108. [CrossRef]